

ARTICLE OPEN



Biocompatible and breathable healthcare electronics with sensing performances and photothermal antibacterial effect for motion-detecting

Xinyi Wang¹, Yan Tao², Shaoshan Pan¹, Xue Fang¹, Congcong Lou¹, Yunqi Xu¹, Jianpeng Wu¹, Min Sang¹, Liang Lu³, Xinglong Gong¹✉, Tianzhi Luo¹ and Shouhu Xuan¹ ✉

With the booming development of smart wearable devices, flexible multifunctional composites with high sensitivity and well health therapy have evoked great interest for next-generation healthcare electronics. However, the weak biocompatibility, low breathability, and narrow sensing range greatly hinder the development of healthcare sensors. Herein, a porous, flexible and conductive MXene/Polydimethylsiloxane/Polydopamine/Polyurethane Sponge (MXene/PDMS/PDA/PU) nanocomposite is developed as a promising motion-detecting device with good flexibility, breathability, sensing performance, photothermal therapy and antibacterial activity. Benefiting from the porous structure and biocompatible surface, this multifunctional sensor is further fabricated into a diagnostic and therapeutic system for monitoring human body motion and performing hot therapy/antibacterial treatment in the application of sports injury site. Moreover, both the wireless smart insole and cushion are constructed to gait monitoring and sit position detecting. This multifunctional hybrid sponge not only demonstrates great potential for motion monitoring sensors but also exhibits wide potential in wearable medical assistive and therapeutic systems.

npj Flexible Electronics (2022)6:95; <https://doi.org/10.1038/s41528-022-00228-x>

INTRODUCTION

During the past decade, the rapid development of wearable electronic devices largely changed human lives. Among various electronic devices, the one endowed with portability, convenience, and close interaction with human activities is urgently required. In daily life, many people often suffer sports injuries, including macro-traumatic injuries causing by strong force and micro-traumatic injuries because of overuse of muscle, joint, ligament, or tendon¹. These injuries generally require long-term medical treatment to ensure them return to a normal life². Typically, correct injury assessment (joint mobility assessment³, etc.), reasonable physical therapy (heat treatments^{4–6}, electrotherapy⁷, etc.), rehabilitation training methods (gait correction training^{8,9}, etc.) and effective means of prevention (injury risk early warning system^{10–12}, etc.) are generally needed. With the development of intelligent wearable devices^{13,14}, healthcare electronics with motion detecting, gesture measuring and injury prevention have been promoted to the direction of normal and personalized. It is reported that the multi-angle fiber arrayed fabric sensor can be applied to precisely measure human joint motion in various degrees of freedom (flexion and rotation) at the shoulders, knees, and wrists in real time¹⁵. In addition, smart strain sensing insoles also have been developed for gait detection in normal training¹⁶.

Wearable electronic sensors with high sensitivity, wide range, quickly response and recovery time have been intensively developed and widely used in monitoring physiological signals such as heart rate, respiratory activity, and muscle tone^{17–19}. With the unremitting efforts of researchers, electronic sensors that can accurately and real-timely detect body motion signal have been mushroomed. Typically, an electronic skin based on a Kirigami-

structured Liquid Metal paper has been developed and it showed both excellent electromyography and electrocardiogram monitoring capabilities²⁰. Moreover, a MXene/ cellulose foam which can real-timely monitor pulse was reported and its sensitivity could reach to as high as 649.3 kPa⁻¹²¹. Besides the sensitive performance, the highly wearing comfort of wearable electronics is essential since long-term and continuous data collecting is required in many practical scenarios²². To our knowledge, most of the wearable monitoring devices still relied on traditional stretchable flexible substrates, such as polydimethylsiloxane (PDMS)^{23–25}, Ecoflex^{26,27}, Polyester (PET)^{28,29} and so on. They were usually bulky and sealed, which reduced the heat and wet comfort of the skin thus further hindered their long-term availability. To improve the wearability of these high-performance sensors, breathable and comfortable nanocomposites have been developed based on nanofiber film³⁰ or textiles^{22,31}. Obviously, as a critical research topic of next-generation healthcare electronics, developing a facile method for breathable, comfortable, and washable strain-sensors is urgently required.

Except for the diagnostic information, an effective management of prevention and immediate treatment during personalized healthcare is also very important for wearable electronic devices³². Heat treatment is a rapid, economical and common treatment for pain relief^{33,34}. It was found that hot pack is of great use for easing muscle tension and treating arthritis³⁵. Therefore, various wearable healthcare electronics have been demonstrated to play a key role in controlled therapy, including electric wristbands for hyperthermia³⁶, triboelectric nanogenerator (TENG) for photothermal therapy³⁷, etc. Moreover, as a kind of skin attachable nanocomposites, the healthcare electronics should also possess good biocompatibility and antibacterial activities. Besides muscle

¹CAS Key Laboratory of Mechanical Behavior and Design of Materials, Department of Modern Mechanics, University of Science and Technology of China, Hefei, Anhui 230027, PR China. ²Outpatient Department, The First Affiliated Hospital of University of Science and Technology of China, Hefei, Anhui 230001, PR China. ³The First Affiliated Hospital of USTC, Division of Life Sciences and Medicine, University of Science and Technology of China, Hefei, Anhui 230036, PR China. ✉email: gongxl@ustc.edu.cn; xuansh@ustc.edu.cn

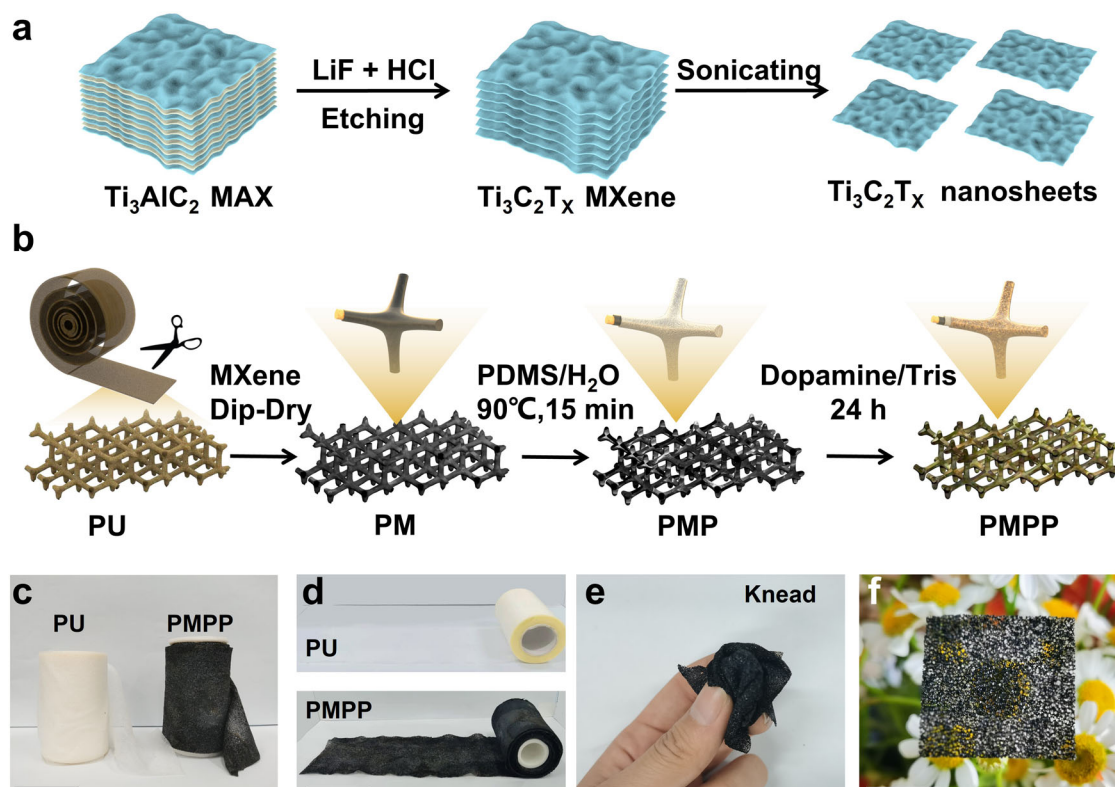


Fig. 1 Scalable manufacturing of breathable PMPP hybrid sponge film. Schematic of preparation process of (a) MXene nanosheets and (b) MXene-based PMPP breathable sponge film. c, d Digital pictures for spools of PU sponge film and PMPP (Scale bars: 3 cm, 5 cm). e Digital picture of kneaded PMPP. f Digital picture of light, porous and thin PMPP (Scale bars: 1 cm).

and skeletal damage, the local epidermal damage occurred during exercise is very susceptible to bacterial infection³⁸. In this case, integrating antibacterial activity to sensors will improve the healthcare performance. By introducing Ag nanoparticles, the epidermal sensors prepared by conductive hydrogels exhibited high antibacterial activity of 99.74% against *Escherichia coli*³⁹ and they could be further applied in as diabetic foot wound dressings. In consideration of that the skin prolonged exposure low biocompatible sensor often leads to dermatitis and microbial infections, the biocompatible, flexible, breathable and washable multifunctional strain-sensor with photothermal hyperthermia and antibacterial effect is undoubtedly a great challenge.

In this paper, a biocompatible and breathable healthcare electronic with outstanding sensing performances and photothermal effect is designed by coating porous Polyurethane (PU) sponge film with MXene, Polydimethylsiloxane (PDMS) and Polydopamine (PDA). Originated from the good electrical conductivity of MXene, the PU/MXene/PDMS/PDA hybrid sponge exhibit a wonderful sensing behavior by distinguishing stretching, low pressure, high pressure and bending stimuli. The conductive MXene and biocompatible PDA synergistically endow the nanocomposite with a high photothermal conversion ability, thus the final healthcare electronics show both a thermal therapy behavior and a photothermal antibacterial effect. To this end, the healthcare electronics attached on the human skin can be applied in not only sensing human activity signals but also thermal therapy at the joints. At last, the wireless smart insole and cushion based on a Bluetooth module are fabricated based on the multifunctional hybrid sponge, which further demonstrate the breathable and biocompatible healthcare electronics possess wide potential in the field of motion-detecting, such as gait detection and sitting posture monitoring.

RESULTS AND DISCUSSION

Preparation and characterization of PMPP porous conductive hybrid sponge film

The delaminated $\text{Ti}_3\text{C}_2\text{T}_x$ was prepared by the minimally intensive layer delamination (MILD) method (Fig. 1a)^{40,41}. Then, these MXenes were assembled onto the surface of PU sponge *via* a facile dip-dry method (named PM). Next, a protective layer is formed by self-crosslinking of PDMS on the PM (named PMP) to prevent the shedding of the MXene layer (Supplementary Fig. 1) and to improve the mechanical properties. Finally, PDA is *in situ* covered on PMP (named PMPP) to increase the biocompatibility of the samples (Fig. 1b). With this simple approach, porous conductive sponge film can be prepared on a large scale (Fig. 1c, d). The sponge film changes from white to black, which must be resulting from the loading of the black MXene and the dark brown PDA. In comparison to the pristine PU, the final PMPP is a little stiffer due to the introduction of inorganic MXene and elastic PDMS. However, owing to the porous structure and lightweight nature, the PMPP is still very soft which endow the product with conformal skin sensing patches (Fig. 1e, f). The conductive MXene nanosheets are assembled on the skeleton of PU sponge, thus the product possesses a good conductivity. Since the electric path is sensitive to the structure, the PMPP can be applied in piezo-resistance wearable sensors to monitor stretching, compression and bending. Moreover, the good photothermal performance of the MXene and PDA also provide the product with photo-thermal hyperthermia and antimicrobial activities for specify body parts.

MXenes is an emerging 2D conductive material based on transition metal carbides and nitrides³⁹. TEM image reveals the slice structure of MXene with an average width of 700 nm, and AFM image measurement indicates the average thickness of nanosheets is 2 nm, which is consistent with the previous reports^{42–44} (Fig. 2a, b). In comparison to the Ti_3AlC_2 , the XRD

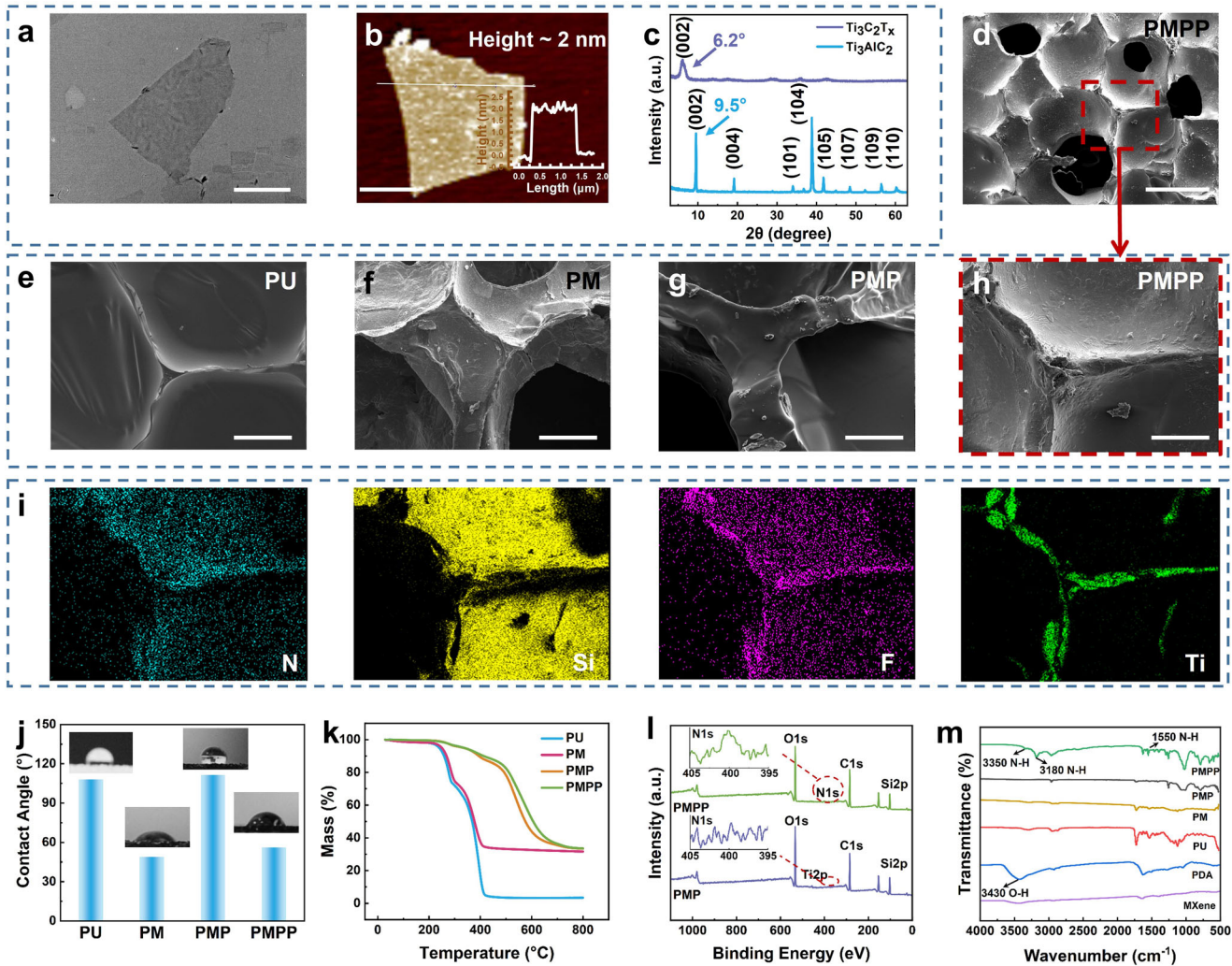


Fig. 2 Characterization of PMPP porous conductive hybrid sponge film. **a** TEM (Scale bars: 400 nm), **b** AFM image (Scale bars: 500 nm) and **c** XRD patterns of MXene nanosheets. **d** SEM image of PMPP (large view) (Scale bars: 500 μm) and enlarged SEM images of **e** PU, **f** PM, **g** PMP and **h** PMPP (Scale bars: 100 μm). **i** N-, Si-, F-, and Ti- element mappings of PMPP. **j** Images and data for water contact angle of PU, PM, PMP, and PMPP. **k** TGA curves of PU, PM, PMP, and PMPP. **l** XPS patterns of PMP and PMPP (Inset: details of N1s curves for PMP and PMPP). **m** FT-IR spectra of MXene, PDA, PU, PM, PMP, PMPP.

strong peak (104) at 39° disappears for the MXene, indicating that the Al layer is completely eliminated. The representative peak (002) at 9.3° moves to a lower angle (7°), indicating that the layer spacing of MXene increases after etching and stripping^{45–47} (Fig. 2c). The above analysis demonstrates the successful synthesis of few-layer or single-layer MXene sheets. Benefiting from the large specific surface area and thin lamina nanostructure, the MXene also exhibits excellent conductivity thus it has been proven to be applied for sensing⁴⁸. The MXene aqueous solution shows a typical Tyndall effect, indicating that MXene nanosheets are well dispersed in water (Supplementary Fig. 2).

SEM images show surface morphology of nanocomposite changes from smooth to rough after being impregnated with MXene. Numerous nanosheets are stacked along PU skeletons and the MXene film is combined by *Van der Waals* force and hydrogen bonding²¹ (Fig. 2e, f). As a complete package layer, the PDMS well protects the MXene layer from falling off (Fig. 2g). Finally, the outside PDA, which can adhere to various object surface, gives a bio-compatible surface⁴⁹ (Fig. 2h). EDS mapping indicates the well encapsulation of the MXene, PDMS and PDA (Fig. 2i, Supplementary Fig. 3). Although the skeleton undergoes PDMS encapsulation and in situ PDA coating, the holes are not blocked, confirming a

good air permeability (Fig. 2d, Supplementary Fig. 4). Benefiting from its porous structure, hydrophilic (Fig. 2j) and elasticity, the sponge provides a good solution for preparing breathable and comfortable sensors^{50–53}.

The TGA analysis (Fig. 2k) indicates that the PU thermal decomposition temperature is 311 °C and the PDMS thermal decomposition temperature is 429 °C. After coating the PDMS, the decomposition temperature increases, proving a high thermal stability for the PMPP. With a low content of PDA on PMPP, a weak N1 peak is found in XPS scanning for PMPP (Fig. 2l, Supplementary Table 1). And new peaks appear in the FT-IR spectra of PMPP (Fig. 2m), 3350 cm^{-1} , 3180 cm^{-1} and 1550 cm^{-1} , ascribed to the stretching vibration and bending vibration of N-H in secondary amide^{54,55}. The significant difference indicates the successful encapsulation of PDA on PMP.

Fabrication and characterization of breathable and flexible PMPPF electrical device

Because of the porous nature and conductive characteristic, the PMPP can be applied as a breathable and flexible sensor. Here, the PMPP is assembled on a pair of copper foil, using silver paste to closely contact the electrode and the sponge to reduce the

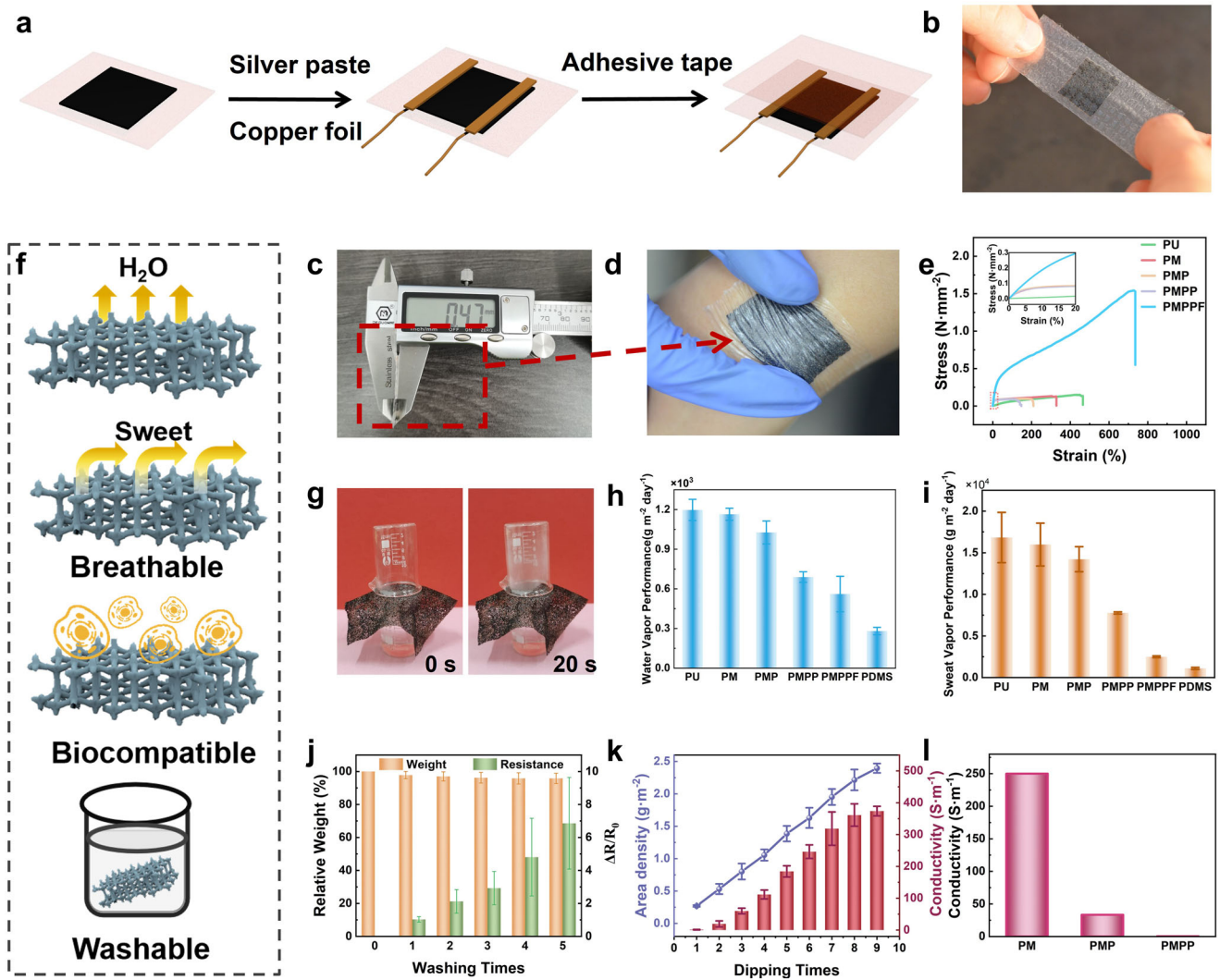


Fig. 3 Fabrication and characterization of breathable and flexible PMPPF electrical device. **a** Schematic preparation process of PMPPF. Digital image of **(b)** PMPPF bandage, **(c)** thickness of PMPPF and **(d)** conformal PMPPF. **e** Strain-stress curves of PU, PM, PMP, PMPP, and PMPPF. **f** Breathable, biocompatible and washable mechanism for the multifunctional flexible sensor. **g** Photograph showing water vapor transmission performance of the breathable hybrid sponge (PMPP). Comparison of **(h)** WVTR and **(i)** sweat vapor performance of different samples (Error bars: s. d., $n = 7$). **j** Evolution of the electrical conductivity of PMPP during washing (Error bars: s. d., $n = 3$). **k** Conductivity and Area density (MXene weight vs Area) of PU dipping with different times of MXene (Error bars: s. d., $n = 3$). **l** Sample conductivity changes of the PM, PMP, and PMPP.

contact resistance. Followed by encapsulation of the sponge unit, the sensor structure is covered by a commercial medical waterproof film and then a light and thin PU/MXene/PDMS/PDA/Film (PMPPF) electrical device is obtained (Fig. 3a, b). The thickness of PMPPF is only 500 μm (Fig. 3c) and the surface density is 9.83 $\text{mg}\cdot\text{cm}^{-2}$, thus this wearable sensor is comfortable. Figure 3e shows the mechanical properties of the PMPPF. The recombination of the medical tape and the porous conductive PMP film greatly improves the mechanical properties of the sensor, enabling it to withstand greater deformation (Supplementary Fig. 5). Clearly, the PMPPF reaches the elastic limit when subjected to a 40% strain, where the deformation can be recovered, proving that the resistance response of the sensor is relatively stable within this strain range. What's more, the Young's modulus is found to be 2 MPa, when the device is attached to the skin, it is very elastic to conform the deformation of skin (Fig. 3d).

Besides the flexibility, the PMPPF also possesses excellent biological compatibility, moisture permeability, and washability, all of them are essential for skin comfort (Fig. 3f). The water vapor transmission rate (WVTR) was measured to evaluate its moisture

permeability^{56,57} (Supplementary Fig. 6, Note 1). Benefiting from the porous structure of sponge film, PMPP demonstrate a wonderful breathability (WVTR = 1026 $\text{g}\cdot\text{m}^{-2}\cdot\text{day}^{-1}$) (Fig. 3g). Obviously, the WVTR of the PMPPF (560 $\text{g}\cdot\text{m}^{-2}\cdot\text{day}^{-1}$) is about twice as much as PDMS film (280 $\text{g}\cdot\text{m}^{-2}\cdot\text{day}^{-1}$) (Fig. 3h), which is large enough as a wearable device compared with previous works (Supplementary Fig. 7, Table 2). The sweet vapor transmission rate (SVTR) of PMPPF is 2503 $\text{g}\cdot\text{m}^{-2}\cdot\text{day}^{-1}$ (Fig. 3i). In contrast, the WVTR of human skin is 200–500 $\text{g}\cdot\text{m}^{-2}\cdot\text{day}^{-1}$ ¹⁵⁶. Therefore, when the PMPPF is attached onto human skin, the skin underneath can breathe normally.

Washability of PMPPF is essential for practical usage. Due to the protection of the PDMS and PDA layer, the resistance change is mainly from the deformation of the sponge structure instead of MXene's fall off (Fig. 3j). Basal conductivity of the PMPPF play a key role in sensing. After dipping six times of MXene, the electrical conductivity of the PM reaches to as high as 246 $\text{S}\cdot\text{m}^{-1}$ (Fig. 3k). With the addition of nonconductive PDMS and PDA, the conductivity of PM inevitably decreases. Finally, the conductivity of PMPP is 0.38 $\text{S}\cdot\text{m}^{-1}$ (Fig. 3l). Thus, the obtained PMPPF sensor

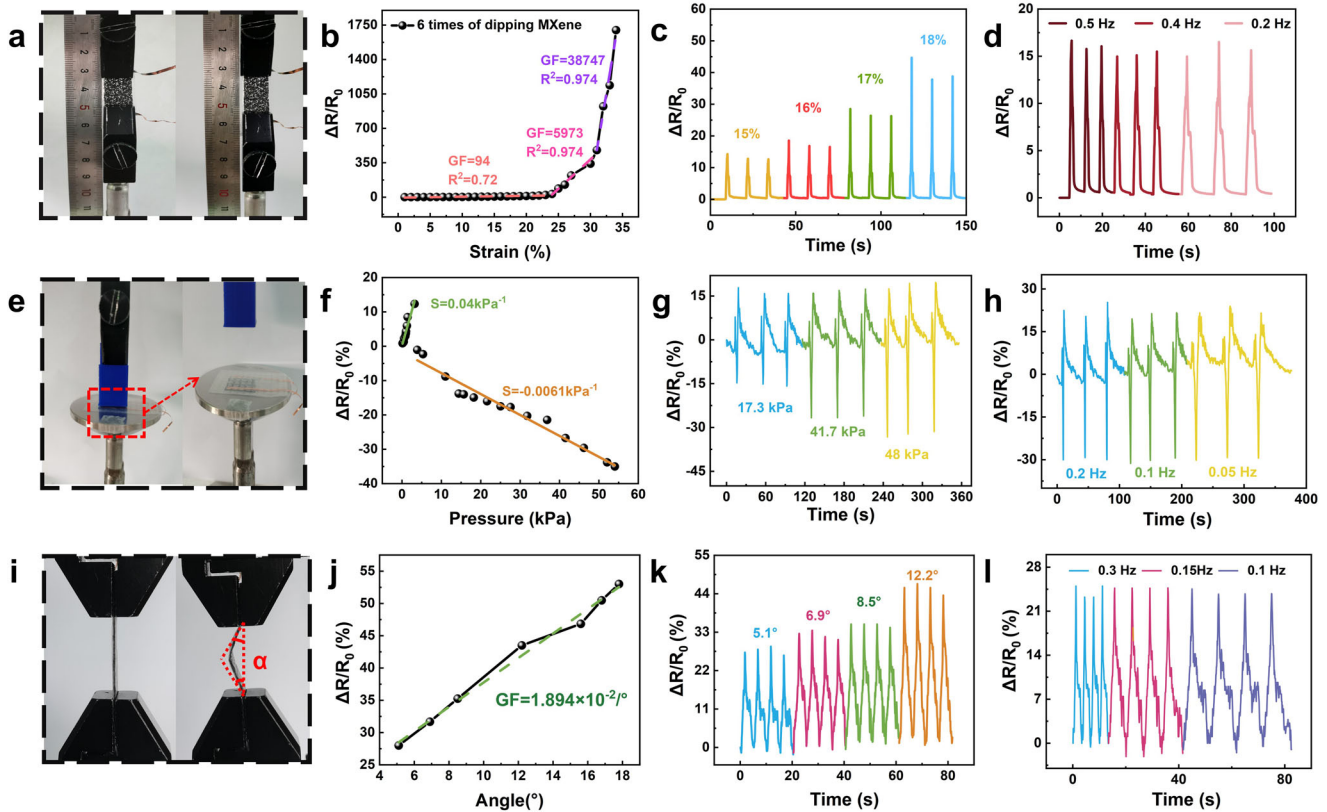


Fig. 4 Sensing property of the PMPPF Sensor. **a–d** Stretching sensor: **a** Digital image of stretching test device. **b** GF of the PMPPF sensor impregnated with the 6 times MXene at different strains (1%–35%). **c** Relative resistance changes of the sensor under stretch-release cycles at a maximum strain of 15%, 16%, 17%, and 18%, respectively. **d** Relative resistance changes of the sensor under stretch-release cycles at 0.2, 0.4, and 0.5 Hz, respectively. **e–h** Compression sensor: **e** Digital image of compress device. Blue column is plastic block (area of thrust surface: 1.5 cm × 1.5 cm). **f** GF of PMPPF sensor impregnated with the 6 times MXene at different pressure (0.13 kPa–53 kPa). **g** Relative resistance changes of the sensor under compress-release cycles at a maximum pressure of 17.3 kPa, 41.7 kPa, and 48 kPa, respectively. **h** Relative resistance changes of the sensor under compress-release cycles at 0.2, 0.1, and 0.05 Hz, respectively. **i–l** Bending sensor: **i** Digital image of bend device. **j** GF of the PMPPF sensor impregnated with the 6 times MXene at different bend angles (5.1°–17.8°). **k** Relative resistance changes of the sensor under bend-release cycles at a maximum bend angle of 5.1°, 6.9°, 8.5°, 12.2°, respectively. **l** Relative resistance changes of the sensor under bend-release cycles at 0.3, 0.15, and 0.1 Hz, respectively.

showing great potential applications in motion-detecting flexible sensors.

Sensing property of the breathable and flexible PMPPF electrical device

The hierarchical structure of MXene layers endow the PMPPF wearable sensor with unique electromechanical properties, thus enabling excellent sensing ability. Here, the strain was controlled by dynamic mechanical analysis (DMA) and the resistance changes of the sensor were monitored with an impedance analyzer (Fig. 4a, e, and i). Low content of MXene often leads to a large resistance of PMPPF (Supplementary Fig. 8a), which will limit the detection range of sensor. The R_0 of sample in 7, 8, 9 dipping times of MXene is lower, but it may reach a plateau of R_0 , which will lead a small ΔR when stretched. Compared with different MXene dipping times, it is found that PMPPF with 6 times of MXene immersion possesses an appropriate GF requirement ($GF = 94$, $1\% < \epsilon < 25\%$; $GF = 5973$, $25\% < \epsilon < 30\%$; $GF = 38747$, $30\% < \epsilon < 35\%$) (Fig. 4b, Supplementary Fig. 8b). Moreover, due to the mechanical hysteresis characteristics (Supplementary Fig. 8e), the PMPPF response quickly (100 ms) but need a long time to recover (5 s) (Supplementary Fig. 8d). When the strain is sustained, the sponge suffers stress relaxation, which causes the resistance first increasing and then decreasing to stabilize during the constant loading (Supplementary Fig. 8f). The PMPPF shows cycling

sensing behavior under different tension (Fig. 4c) and frequencies (Fig. 4d). Obviously, PMPPF exhibits a good recoverability under different strain, in which the response first goes up and then goes down (Supplementary Fig. 8c), and shows stable signal output during 1000 cycles stretching (Supplementary Fig. 8g).

Interestingly, the resistance change of the PMPPF shows a strain-dependent nature when the pressure signals is monitored. The response time of PMPP pressure sensor is 300 ms (Supplementary Fig. 9a) and detection limit is 0.1 kPa. The resistance of the PMPPF increases when subjected to low pressures (0.1–3.5 kPa) and decreases under high pressures (3.5–60 kPa) (Fig. 4f). PMPPF exhibit unique resistance responses at high pressures (Fig. 4g). Details shown in Supplementary Fig. 9b demonstrate that when the sensors are pressed heavily, their resistance increases slightly and then immediately decreases, which is due to the fact that the sponge must be subjected to the low pressure first during the process of receiving the high pressure. As pressure is released, the sponge bounces back, which leads to resistance change increase to positive value, and gradually returns to the initial value again after a period of time⁵⁸. Supplementary Fig. 10 shows strain sensor under low pressures (0.1, 0.3, 0.44 kPa) have a stable signal output. In addition, the sensor exhibits stable and robust electrical signals within pressing and releasing cycles even at different frequencies (Fig. 4h).

To more comprehensively characterize the mechanic sensing properties of the sensor, the PMPPF responses under bending

stimuli is also investigated. PMPPF has high sensitivity within 18° of bending angle ($GF = 1.894 \times 10^{-2}/^\circ$) and show a quick response (100 ms) (Fig. 4j, Supplementary Fig. 11a). Moreover, the PMPPF exhibits stable and robust electrical signals within bending and releasing cycles (Fig. 4k, l, and Supplementary Fig. 11b, c). Compared with the other sensors in the literature, PMPPF has high sensitivity, wide range, quickly response thus possesses great potential in practical applications (Supplementary Fig. 16, Table 3).

Sensing mechanism of the breathable and flexible PMPPF electrical device

The schematic diagram in Fig. 5 explores the detailed sensing mechanism. An optical microscopy was used to observe the deformation during stretching/compression and finite elements simulation has been invited to simulate the stress process. For stretch-sensing mode, the different sensitivity at low and high strain is the result of the porous structure of the sponge. At low strain, a stress concentration occurs at the angle of the hexagonal structure of the sponge and tiny cracks will be created at the MXene conductive layer attached on the skeleton. Therefore, a slight deformation of the sponge structure result in a slight rise of resistance. When a high strain is applied, the sponge skeleton has a large tensile deformation, causing a further separation of MXene conductive layer. Therefore, the electric resistance changes greatly under the large deformation (Fig. 5a–c, and Supplementary Videos 1, 3).

Figure 5d illustrates the corresponding schematic evolutions of the sensor under pressure-sensing mode. At first, the finite element simulation proves that the stress is mainly concentrated at the skeleton joints when the structure is applied a small compressive strain. So, the detachment of MXene nanosheets at deformation of the sponge skeleton reduces the conductive pathway and leads to the rapidly increase of the resistance in the sensor. As the pressure increases to a critical value (3.5 kPa), the upper spongy skeleton is squashed, and it contacts to the lower layer due to the structure instability. Hence, the MXene layers will be connected continuously with each other and the conductive path increase (Fig. 5e, f, and Supplementary Videos 2, 4). At this time, reduced contact resistance of sponge skeletons turns into the main cause for the resistance change of the sensor, resulting in a sharp decrease in resistance. As a result, the PMPPF sensor can distinguish the low and high pressure, which has not been well discussed in the previous work.

The bending-sensing mode is similar to the stretching-mode. This is mainly due to the thin PMPPF film sponge was posted on outside PDMS film. When PDMS bending to outside, PMPPF is stretched (Fig. 5g–i), which reduces the conductive paths, correspond to the increased electrical resistance (Supplementary Video 7).

Photothermal heating performance of the PMPPF hybrid sponge

Besides the diagnostic function, the therapeutic system will also benefit a wearable sensing platform with the therapeutics to reduce the health risk of the patient⁵⁹. The hyperthermia is very important for treating the sport damage. Due to the presence of MXene and PDA, the PMPP hybrid sponge also exhibits excellent near-infrared (NIR) photothermal heating characteristic (Fig. 6a).

Figure 6b presents the normalized Ultraviolet-vis-NIR absorbance of PDA, MXene and PDA/MXene aqueous dispersions, respectively. Both MXene and PDA/MXene nanocomposites exhibit prominent absorption in the region of 700–850 nm. It is reported that MXene has a higher photothermal conversion efficiency compared to PDA⁶⁰, thus MXene is the main material for producing the photothermal effect. Obviously, the photothermal energy conversion performance of hybrid sponge film enlarges with an increasing dipping amount of MXene (Fig. 6c). After 6 times of coated MXene, PM reveals a satisfying photothermal

conversion performance at low power density (83 °C at 0.19 W·cm⁻²). As shown in Fig. 6d, after 70 s lighting, the peak temperature of the PU/PDA (PP), PM, PMP, PMPP, and PMPPF rises to 60 °C, 83 °C, 83 °C, 75 °C, and 75 °C, respectively. Although PDA did not produce synergistic effect with MXene, it did not significantly reduce the photothermal effect. Besides, the transparent PDMS and medical tape don't affect the heating capacity of the whole sample. The photothermal conversion efficiency of the PMPPF reaches 23.99% (Supplementary Note 3).

With the elevation of the NIR laser power densities, the surface temperature of PMPPF gradually increases. For instance, when exposed to continuous NIR irradiation of 0.22 W·cm⁻², the surface temperature of the PMPPF increases drastically from 25 to 80 °C within 40 s and reaches an ultrahigh equilibrium temperature of 90 °C in 75 s. After the removal of the light source, its surface temperature quickly drops back to room temperature (Fig. 6e). Interestingly, there is a good linear relationship between saturation temperature and power density. Therefore, the desired surface temperature can be obtained by controlling power density (Fig. 6f). The heater also demonstrated stable cycling performance as shown in Fig. 6g. Infrared thermal images intuitively reveals PMPP is able to respond rapidly to near-infrared light in a short time, while the PU sponge used as a control shows no temperature change. In comparison to the PMP, the highest temperature of PMPP is lower, which is consistent with above thermocouple results (Fig. 6h). Compared with xenon lamp irradiation, NIR light could heating the PMPPF faster and higher (Supplementary Fig. 12).

It is found that MXene is used for temperature sensing and its resistance decreases versus increasing temperature^{61,62}. This phenomenon can also be observed in Supplementary Fig. 13c. As shown in Supplementary Fig. 13a, b, the resistance decreases with the increase of NIR light power density, which is due to the increasing temperature of PMPPF. In addition, PMPPF returns to the initial resistance after a long time of cooling, which will not affect the subsequent force sensing monitoring. In a word, the results show that PMPPF has excellent photothermal conversion capability, stability and controllability as a photothermal device. These advantages enable its application in medical treatment, such as arthritis treatment, promote wound healing and so on.

Biocompatibility and photothermal antibacterial activity of electrical device

Although the PDA decrease the photothermal effect, it improves the biocompatibility of the final PMPP. As a healthcare electronic, biocompatible surface and antibacterial characteristic play very important roles in preventing infection and providing adjuvant treatment in practical use. In particular, PMPPF often closely contacts with the skin, its biocompatibility and antibacterial properties are even more necessary to be characterized.

The quantification of cell viability experiments (MTT) detected by the microplate reader shows that relative viability of cells cultured by PMPP leach liquor is 69.6%. The biocompatibility of the material is considered qualified combined with the cell morphology analysis, which proving the addition of PDA can enhance the cell compatibility of the material (Fig. 7a, and Supplementary Tables 4, 5). For live/dead cell staining, live cells are stained green. Figure 7b shows the normal cell morphology of cells with pseudopodia in the blank control group. However, due to the cytotoxicity of PMP, abnormal cell morphology is observed in Fig. 7c. Fortunately, there are normal cell morphology in Fig. 7d, qualitatively demonstrating that the PMPP is biocompatible. In order to further prove that it is not harmful to human body, the volunteers wore the sample on the forearm for a week, and the skin is not red, swollen and itchy after a week, which prove that PMPPF has no skin irritation (Supplementary Fig. 14).

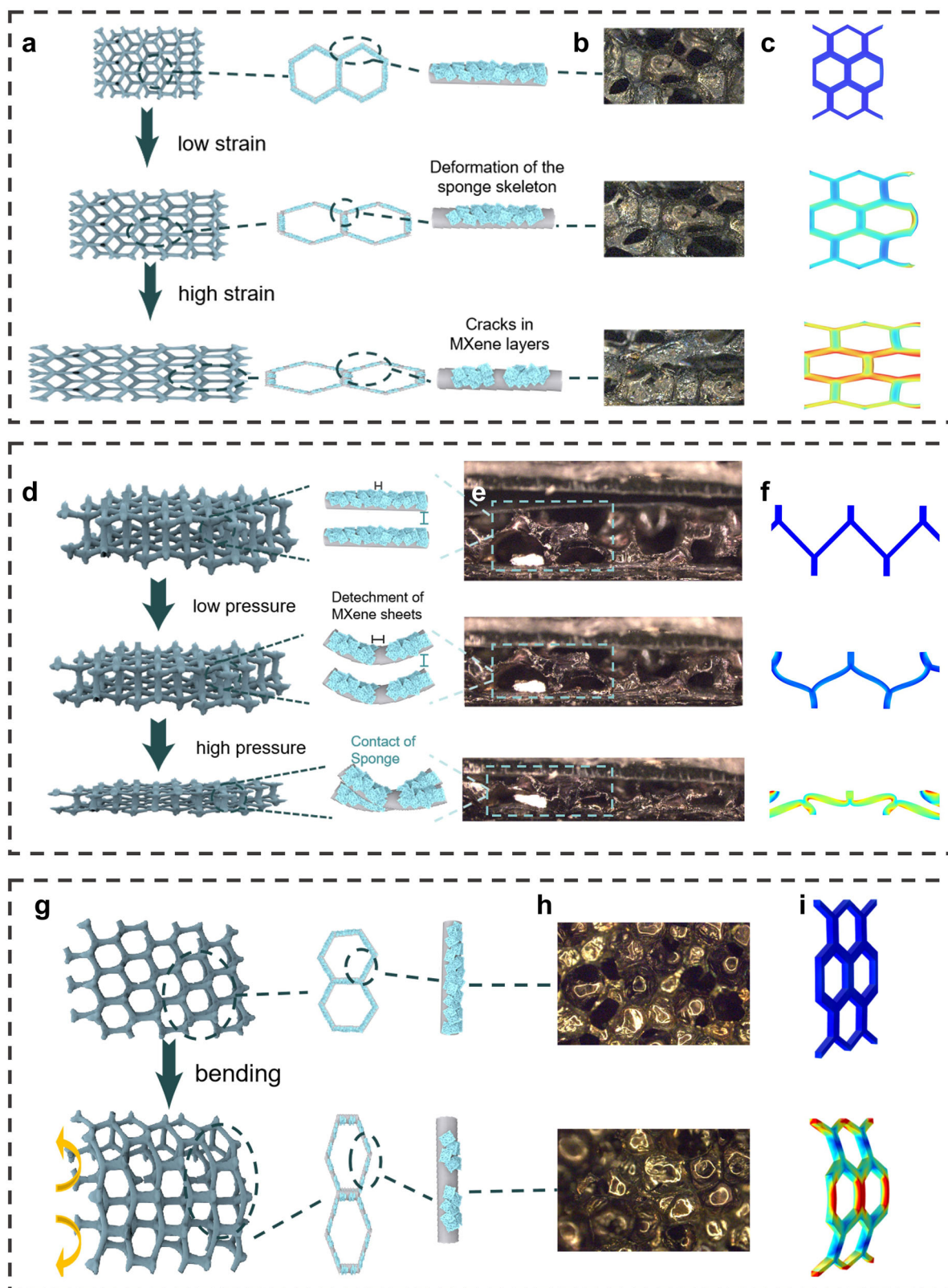


Fig. 5 Working mechanism of the PMPPF electrical device. **a–c** Stretch modes: **a** Schematic of sensor under low strain and high strain. **b** Optical microscope images of stretched sensor from surface topography. **c** Finite element simulation of the stretching process. **d–f** Compression modes: **d** Schematic of sensor under low pressure and high pressure. **e** Optical microscope images of compression sensor from cross section topography. **f** Finite element simulation of the compression process. **g–i** Bending modes: **g** Schematic of sensor under bending. **h** Optical microscope images of bending sensor from surface section topography. **i** Finite element simulation of the bending process.

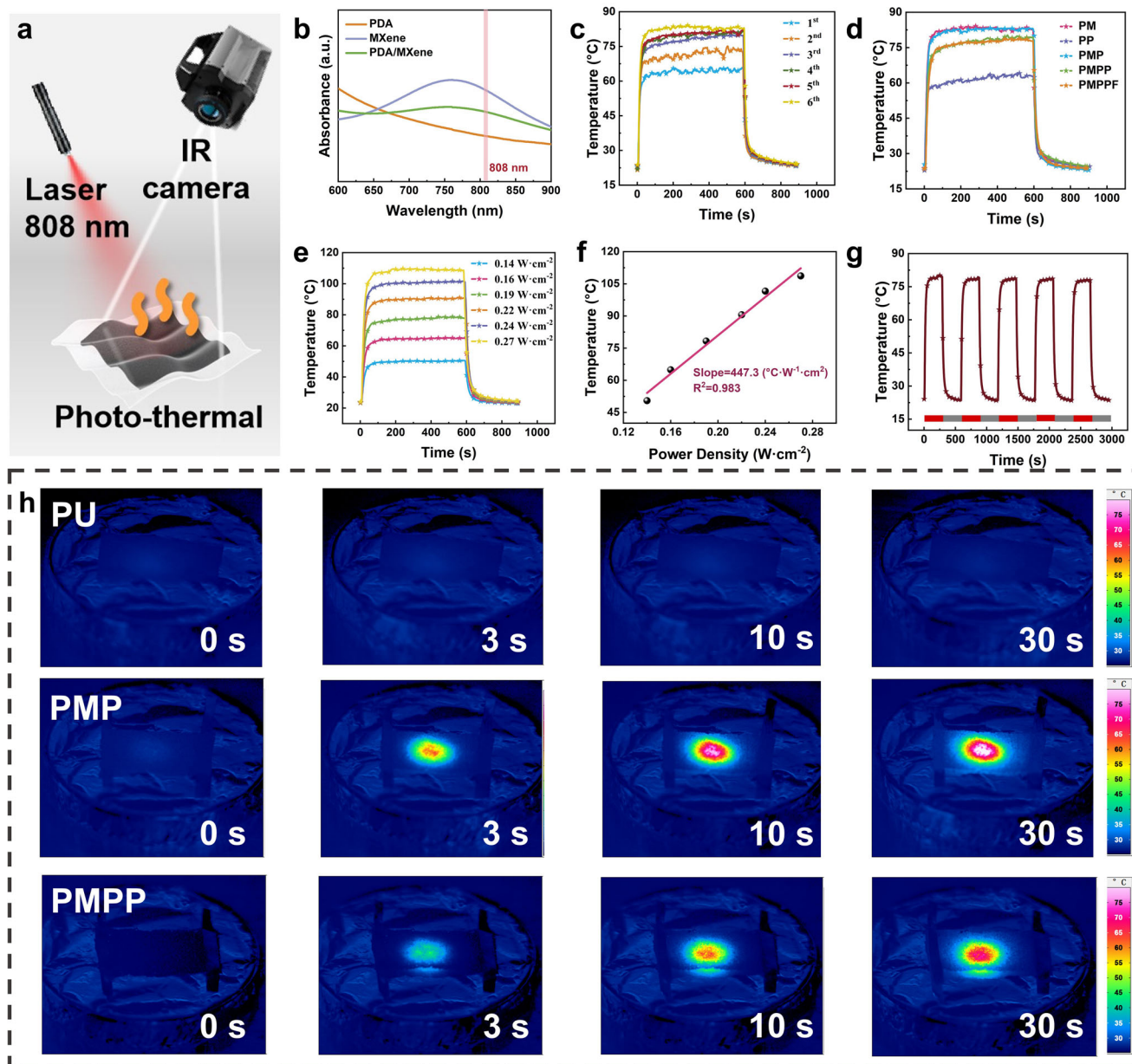


Fig. 6 Photothermal heating performance of PMPPF electrical device. **a** Schematic diagram of simulated photo-thermal test model. (Laser height = 10 cm) **b** Ultraviolet-vis-NIR absorbance of PDA, MXene and PDA/MXene nanocomposites aqueous dispersions. **c** The temperature-time curve of PM prepared with different MXene coating times. **d** The temperature-time curve of PP, PM, PMP, PMPP, and PMPPF. **e** The temperature-time curve of PMPPF (lower surface) under different power densities and **f** corresponding linear fitting curve of the relationship between equilibrium temperature and NIR laser power densities. **g** Temperature curves for 5 laser on/off cycles. **h** IR images of PU, PMP, and PMPP (Power density = $0.19 \text{ W}\cdot\text{cm}^{-2}$).

Meanwhile, the photothermal effects of the PMPPF can be further used in antibacterial due to the low heat resistance of bacteria^{63–65}. Here, Gram-negative bacteria *Escherichia coli* (*E. coli*) and Gram-positive bacteria *Staphylococcus aureus* (*S. aureus*) are selected to explore the antibacterial properties of PMPPF in two dimensions of time gradient (Power density = $0.27 \text{ W}\cdot\text{cm}^{-2}$) and power density (Light duration = 20 min). The antimicrobial data for the samples are detailed in Supplementary Table 6. Significant inactivation is observed of PMPPF against *S. aureus* and *E. coli* (99.998% and 99.998%, respectively) after 20 min of infrared light at $0.27 \text{ W}\cdot\text{cm}^{-2}$ power density (Supplementary Table 6). The excellent photothermal conversion efficiency causes PMPPF to have a good bactericidal effect in a lower power density and a faster time (Fig. 7e–h). The colony optical photos can more directly

show the excellent antibacterial performance of PMPPF (Fig. 7i). As shown in SEM images, obviously, after NIR treating, significant crinkling and outflow of contents are observed in both *E. coli* and *S. aureus* (Fig. 7j–m). PMPPF with photothermal antibacterial action provides a new approach to human antimicrobial therapy and promotes the development of the next generation of multifunctional wearable medical monitoring devices.

A diagnostic and therapeutic system with multifunctional device

Based on the unique electromechanical properties of PMPPF and its excellent photothermal and antibacterial properties, a set of medical strategies capable of assisting motion diagnostics and

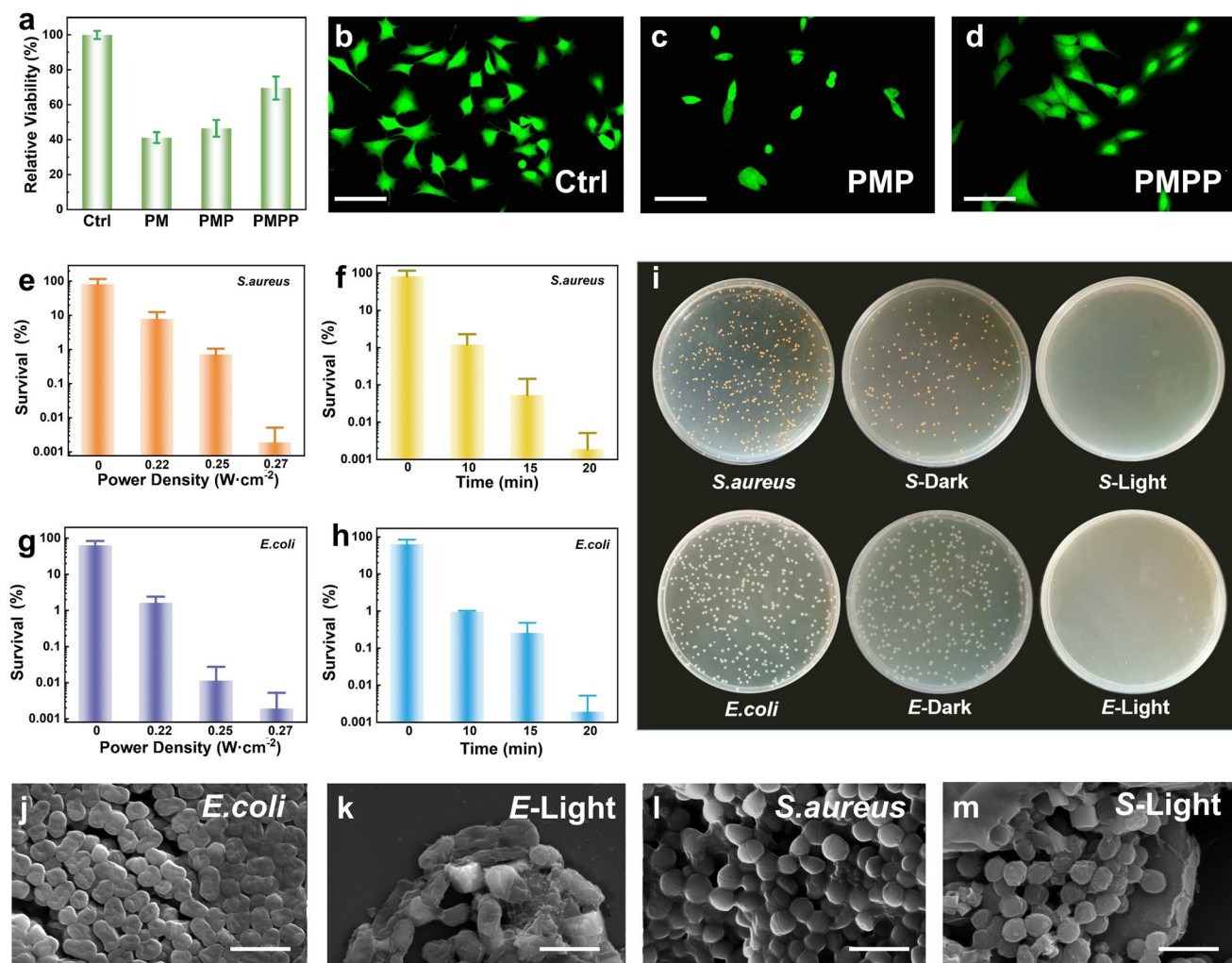


Fig. 7 Biocompatible and photothermal antibacterial performance of PMPPF electrical device. **a** Cell relative viability of NIH-3T3 cells treated by different samples (Error bars: s. d., $n = 6$). Typical fluorescence microscopy image of mouse cells (NIH-3T3) after incubation for 1 day on the substrate of **b** Control, **c** PMP and **d** PMPP (Scale bars: 10 μm). Survivability of **e** *S. aureus* and **g** *E. coli* after treatment with PMPPF under different power densities of IR laser. (Irradiation time = 20 min). Survivability of **f** *S. aureus* and **h** *E. coli* after treatment with PMPPF under different irradiation times of IR laser. (Power density = 0.27 $W \cdot cm^{-2}$). **i** Digital images of agar plates used for the growth of *E. coli* and *S. aureus* exposed to PMPPF for 20 min under conditions with or without NIR (808 nm) laser irradiation. SEM images of untreated **j** *E. coli* and **l** *S. aureus*. SEM images of **k** *E. coli* and **m** *S. aureus* after treated with PMPPF. (Scale bars: 2 μm).

therapeutics are proposed. Body signal monitoring during motion and joint motion assessment are assisted by the force sensor. Through the photothermal conversion effect, the injured muscles and joints can be heated at a fixed point, and the temperature can be adjusted according to the infrared light radiation area and power. At the same time, the wounded part can be sterilized by heat (Fig. 8a).

After being pasted onto the skin, the PMPPF can monitor various deformations generated from human activities. For example, sensors can monitor large deformation, such as fingers and wrist bend. Different degrees of bending angles can be effectively monitored, indicating it shows a high potential in detecting human joint motion (Fig. 8b, c). When the PMPPF is pasted on the wrist, cheek and throat, small deformation also can be monitored. It can well distinguish the arm muscles movement when clenching fists with different strength, meaning that it can be applied to monitor the muscle strength of patients (Fig. 8d). The sensor can also monitor a human swallowing signal, and the waveform of the signal is basically unchanged when the swallowing is repeated for five times (Fig. 8e). When the mouth is open and closed, two peak electrical signals can be detected

(Fig. 8f). Moreover, the sensor also can respond to blowing, demonstrating its potential in respiration detection (Fig. 8g). Most importantly, the medical monitoring system also can be applied for hyperthermia therapy due to its wonderful photothermal properties. As a result, the device is pasted on the wrist, neck, elbow and other areas prone to joint injury and muscle strain. Through infrared light irradiation, the temperature of PMPPF can reach to about 50 °C, which is high enough for the thermotherapy (Fig. 8h–j). Based on the analysis, it can be concluded that this medical monitoring system will play a good role in motion-detecting and hot therapy applications.

Wireless real-time foot pressure mapping system

Furthermore, the Bluetooth module is connected to the PMPPF sensor to transmit the signals into the mobile phone terminal to realize a wireless flexible healthcare system (Fig. 9a). As shown in Fig. 9b, the resistance changes of one PMPPF sensor under different compression can be transferred and showed in mobile phone. Furthermore, the sensors can be assembled into an integrated array such as wireless flexible sensing insoles to detect the stress and strain (Fig. 9c).

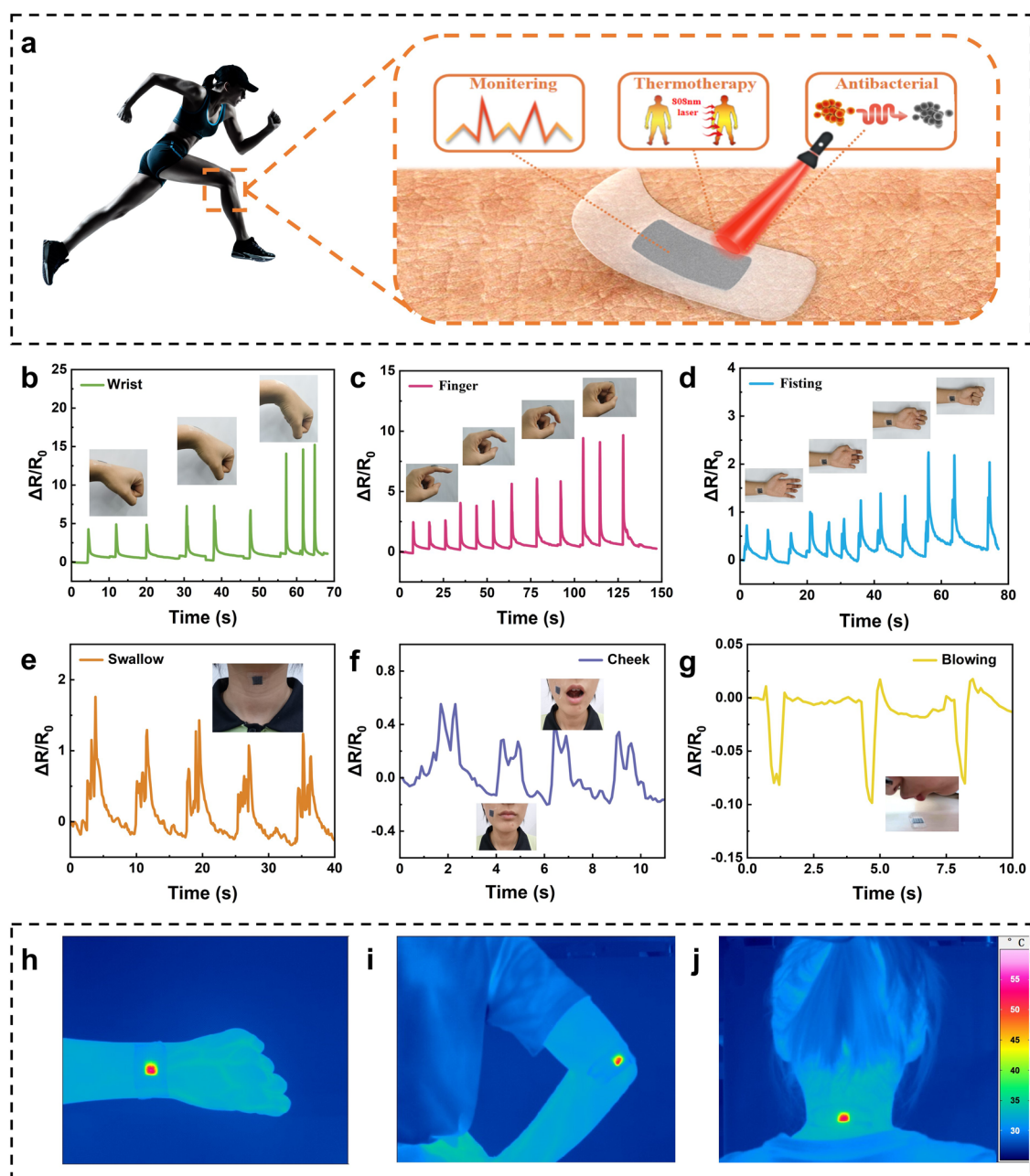


Fig. 8 Multifunctional device for sports rehabilitation medical. **a** Schematic illustration showing an integrated multifunctional sensing system (sensing, heat treatment and sterilization) for sports rehabilitation. Resistance variation of PMPPF sensors when monitor large body deformation, such as **b** wrist and **c** fingers bend. Insets: digital images of the wrist and index finger at different angles. Resistance variation of PMPPF sensors when monitor small body deformation, such as **d** fisting, **e** swallow, **f** mouth open/close and **g** blowing. Insets: digital images of different stages of fist clenched, swallow, mouth and blowing. IR images of PMPPF sensor under infrared light at 50 °C for hot application on the **h** wrist, **i** elbow, **j** neck.

25 sensor units are pasted in two ultra-thin insoles to develop a continuous and real-time pressure distribution monitoring system (Fig. 9d, Supplementary Fig. 15). Two common walking postures, the out-toe and in-toe, are imitated to reflect the plantar compression through ΔR at the five monitoring sites. Clearly, the inside of the footprint of toe in waking habit is deeper, indicating these parts maintaining larger compression forces (Fig. 9e). As for walking of toe out, the outside of the footprint receives a larger pressure.

In addition, four channels on the sensing insole are selected to show the tested result for pressure signal in different parts of the foot during one walking cycle. During one walking cycle, the foot

force point moves from the heel through the arch and the first metatarsal to the tip of the thumb. Correspondingly, the response times of these four monitoring sites are obviously different (Fig. 9g). The response at the sensor of heel is clearly earlier than the others. Meanwhile, the output $\Delta R/R_0$ signal can demonstrate the size of the plantar force. Supplementary Video 5, Fig. 9f and h display the mechanical signal of walking cycles transmitted by a wireless Bluetooth sensing unit, showing the possibility of PMPPF as a gait monitoring device. In general, this wireless monitoring system can provide a feasible strategy for real-time foot pressure mapping, injury prevention, and ulceration prediction in the feet.

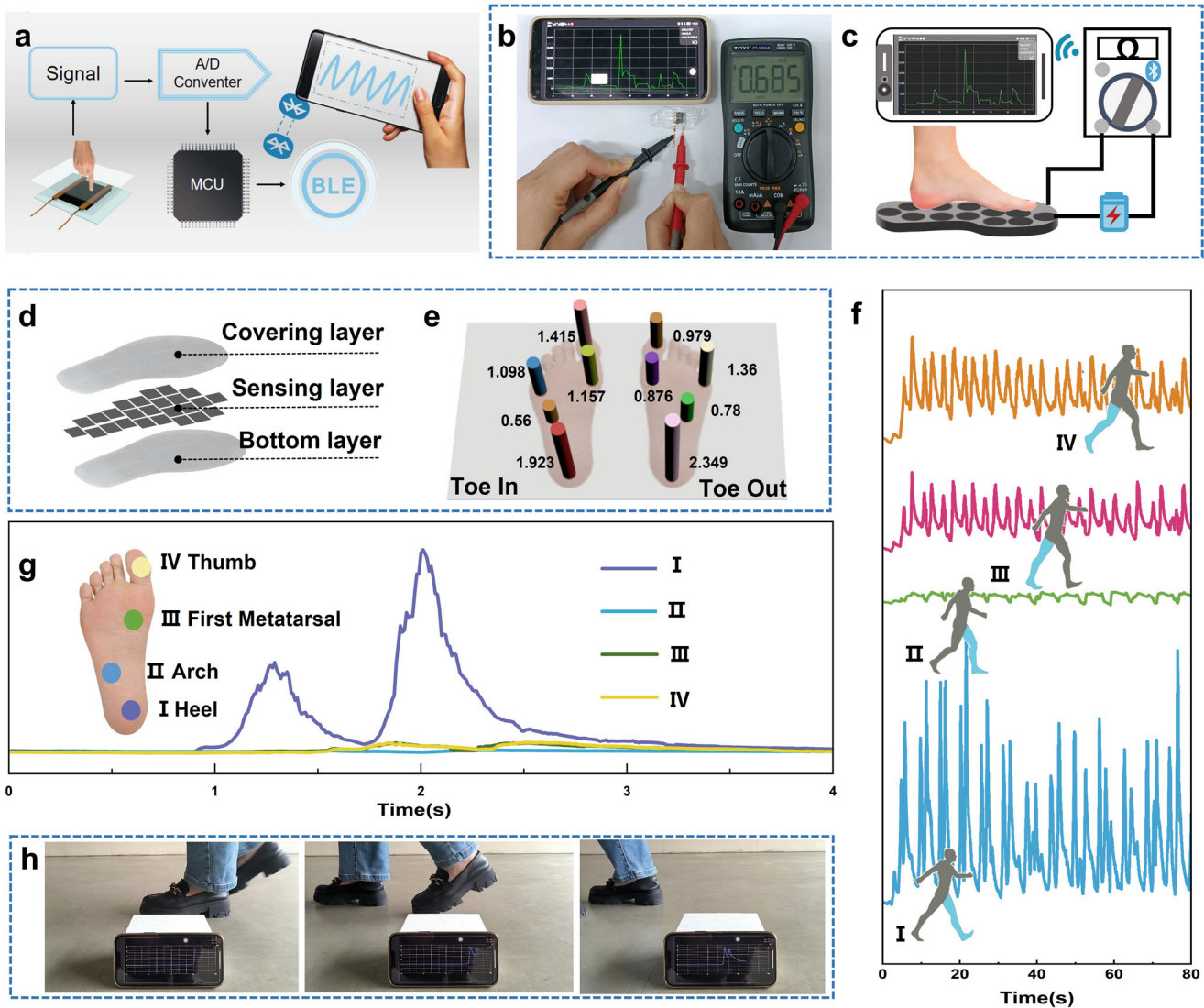


Fig. 9 Wireless real-time foot pressure mapping system. **a** Schematic diagram of the Bluetooth transmission mode. **b** Physical picture of the Bluetooth signal transmission of one single sensor. **c** Schematic diagram of a wireless smart insole based on a Bluetooth module. **d** Schematic diagram of the smart insole. **e** Histogram of Toe-in and Toe-out signals monitored by the smart insole (five detection points). **f** Signals of walking cycles measured at the four monitoring points. (From bottom to top are the heel, arch, first metatarsal and thumb). **g** Signals of one walking cycle. **h** Digital images of wireless smart insoles for one walk cycle.

Wireless smart cushion system in detecting sitting postures

In addition, PMPPF can be fabricated as wireless smart cushion to monitoring sitting posture (Fig. 10a). In order to ensure the softness of the whole sensor device, the commercial conductive silver yarn is used as the electrode to sew the sensor to the non-woven cushion (Fig. 10b). When sitting on the 4×5 PMPPF sensor array, different sensing cells will feel different pressures and produce different resistance changes.

The resistance variation value for each cell can be drawn into a cloud map of the pressure distribution. When the volunteer sits flat on the smart cushion, the barycenter is in the center of cushion because the spine remains neutral (Fig. 10c). Figure 10f, h show that the force is symmetric along the y-axis, corresponding to the two legs of the person. When the volunteer crossed his legs (Fig. 10d), the center of gravity is greatly shifted. In this position, the force on both sides is unbalanced and the pressure is concentrated on one leg (Fig. 10g, i). Clearly, this smart cushion can be used as an adjunct to sitting posture correction in rehabilitation patients. Thus, the cushion can be used for wrong

sitting position alarm, as shown in the flow chart (Fig. 10e). When changes to the wrong posture, the resistance of a certain sensor will decrease due to the pressure increase. So, it could just set the highest resistance limit (R_{High}) of the alarm. If $R > R_{High}$, mobile phone will alarm to remind the volunteer to change the sitting position (Supplementary Video 6). Base on this smart cushion, smart mattress systems can also be developed for sleep monitoring in the future.

In a word, this work reports a multifunctional breathable, washable, biocompatible, soft, porous healthcare wearable sensor prepared by integrating porous PU sponge film with MXene, PDMS, and PDA as conductive layer, protective layer and biocompatible layer, respectively. The sensor packaged by a medical film has quick responds to pressure, tensile, and bending stimuli. It is worth mentioning that the hybrid sponge sensor has an excellent tensile sensitivity of $GF = 38747$ and a wide sensing range ($\varepsilon < 35\%$) to precisely monitor biological activities of the human body. Typically, the shell-shaped stacked MXene conductive layer on the PU sponge skeleton exhibits separation or

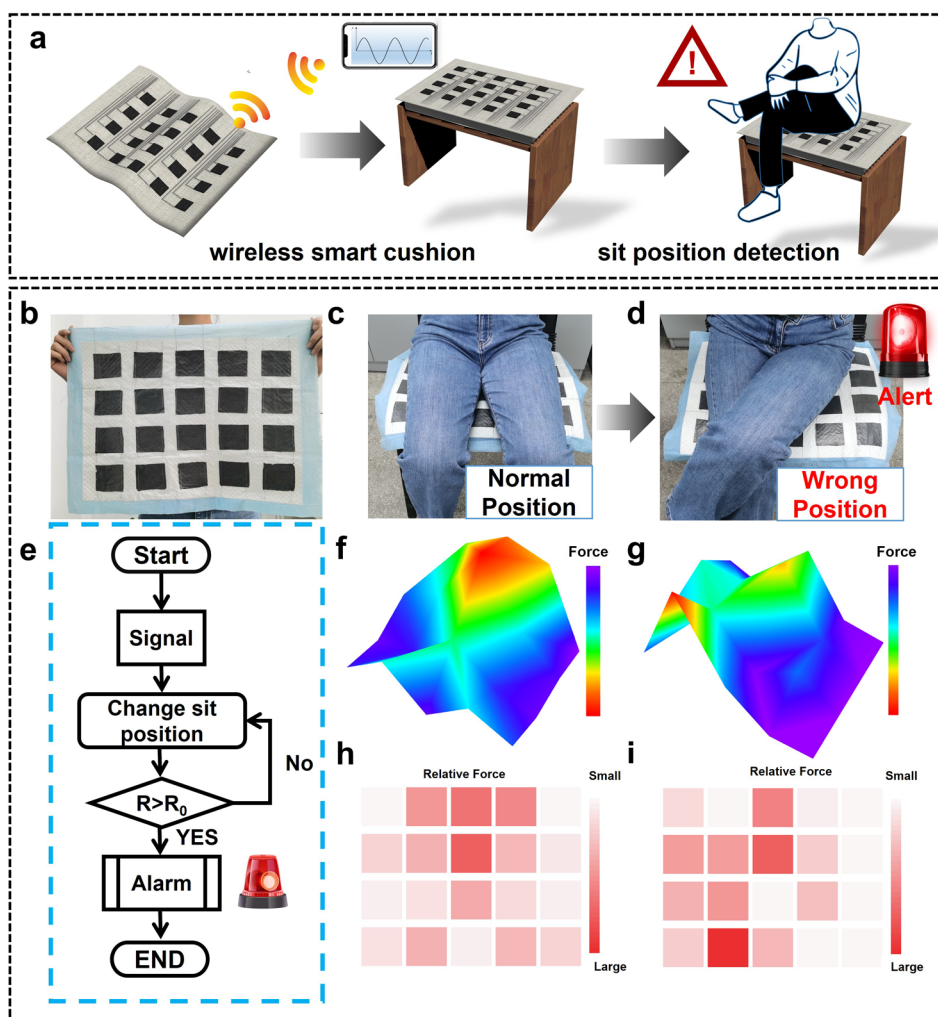


Fig. 10 Wireless smart cushion system in detecting sitting postures. **a** Schematic diagram of wireless smart cushion system. **b** Digital image of smart cushion. (45 cm × 60 cm, 4 × 5 arrays). Digital image of detecting sitting postures at **c** normal position and **d** wrong position. **e** Flow chart of the wrong sitting position alarm principle. Cloud map of **f** normal and **g** incorrect sitting obtained from detection points. Thermal map of **h** normal and **i** incorrect sitting obtained from detection points. The data indicate the relative pressure converted by the change in resistance.

contact when subjected to tension and pressure, thus contributing the sensor with a bidirectional resistance change to distinguish low pressure, high pressure and strain. Moreover, PMPP exhibits excellent NIR photothermal effects (rose from 25 to 80 °C within 40 s under NIR light illumination) and antibacterial properties (99.998% against *E. coli* and 99.998% against *S. aureus*). Based on the multifunctional sensors, a multimodal smart system composed of strain sensing and photothermal treatment is fabricated and it shows the potential of human exercise signal monitoring and exercise physiotherapy. Furthermore, integrated sensing units equipped with a Bluetooth module to a wireless smart insole can monitor out-toe and in-toe. Then a false sitting position alarm is constructed based on the homemade wireless smart sensing cushion. As a result, due to its green process, scalable preparation, and attractive features including good durability, excellent comfortability, and multifunctionality, PMPPF wearable sensor is a promising candidate for fabricating breathable smart systems for motion-detecting healthcare devices. In the future, using data analysis and machine learning technology, smart insole and cushion array can be further used for gait clinical diagnosis of knee arthritis patients, fall warning and so on to realize introducing the

Internet of things into personalized smart medicine to promote the health management of users.

METHODS

Materials

Commercially available PU sponge film (width = 7 cm) were purchased from Suzhou Shutao Medical Supplies Co., Ltd. (China). Medical tapes were bought from Smith&nephew (UK). The PDMS (type Sylgard 184) were provided by Dow Corning GmbH (USA). Ti₃AlC₂ MAX (400 meshe size) was obtained from 11 Technology Co. Ltd. (China). Lithium fluoride (LiF) was purchased from Aladdin chemical Co., Ltd. (China). Chemicals including Trihydroxymethyl Aminomethane (Tris), Dopamine Hydrochloride (DA-HCl), Hydrochloride (HCl), Ethyl alcohol (EtOH) were supplied by Sinopharm Chemical Reagent Co., Ltd. (China). Artificial sweat (PH = 4.7) was obtained from Dongguan Chuangfeng Automation Technology Co., Ltd. Luria-Bertani Broth and Luria-Bertani agar were provided by the Hangzhou Microbial Reagent Co., Ltd. (China). *E. coli* (CMCC 44102) and *S. aureus* (CMCC 26003) were used for antimicrobial testing. Fetal Bovine Serum was purchased by Biological Industries Co., Ltd. (Israel). Cell counting kit-8 (CCK-8) was provided by Dojindo

Laboratories (Japan). DMEM was obtained from Gibco Co., Ltd. (China). NIH-3T3 cell line was used for biocompatibility evaluation. Deionized (DI) water is used throughout the experiment.

Preparation of MXene nanosheets

The delaminated $\text{Ti}_3\text{C}_2\text{T}_x$ was prepared by the minimally intensive layer delamination (MILD) method^{40,41}. Specifically, Al layer was etched from Ti_3AlC_2 MAX phases with LiF/HCl. Firstly, a concentrated hydrochloric acid was diluted in distilled water to obtain a 9 M HCl solution. Then, 2 g LiF was added to 40 mL 9 M HCl solution followed by stirring for 30 min until LiF was dissolved. Next, 2 g Ti_3AlC_2 powder was added to 35 °C etching solution and reaction was stirred constant for 24 h. Then, the resultant slurry was repeatedly washed and centrifuged at 3500 rpm until pH ≥ 6 . The lower layer of precipitation was collected and ultrasonically exfoliated in an ultrasonic machine for 2 h. The suspension was transferred to the centrifuge, centrifuged at 3500 rpm for 2 h. Finally, the supernatant of $\text{Ti}_3\text{C}_2\text{T}_x$ nanosheets was obtained.

Preparation of PMPP

First, the purchased PU sponge film was dipping in the above synthetic MXene solution, then dried in the vacuum oven at 60 °C for 15 min. The processes of soaking and drying were repeated to obtain PU-MXene with different MXene contents (named as PM). Second, the mixture of 0.1 mL PDMS and its curing agent (A/B = 10/1, wt/wt) was absorbed by a needle and placed on the surface of DI water (DI water was placed in a 9 mm petri dish). The PDMS mixture was evenly dispersed by surface tension. Then, the PM was placed on the page, the PDMS solution was absorbed and turned over PM until PDMS was evenly absorbed. After that, the PM/PDMS (PMP) was transferred into the oven at 90 °C to curing PDMS for 30 min. Third, the PM/PDMS was impregnated for 24 h in an aqueous solution of dopamine hydrochloride (2 g·L⁻¹) and tris buffer (10 mM, pH 8.5). At last, PM /PDMS-PDA (PMPP) was cleaned with DI water and dried in oven at 50 °C.

Fabrication of PMPP based pressure strain sensor (PMPPF)

The prepared sample was placed on a transparent medical dressing with a pair of copper wires as electrodes and pasted with silver paste. The sensor is then secured with an appropriately sized elastic medical transparent dressing.

Fabrication of smart insoles and cushion

Fabrication of sensing insoles: firstly paste 25 2 × 2 cm sensors on one insole and then cover the sensor with another thin insole to protect the array.

Fabrication of sensing cushion: first, cut PMPP into unit with size of 5 × 5 cm. Second, commercial conductive silver yarn (200 D) was used as a flexible electrode to sew PMPP onto one-time care pad (45 × 60 cm, Nantong Anyi sanitary products Co., Ltd. China). Finally, medical tape was pasted onto the PMPP to protect the sensors.

Fabrication of wireless sensor system: Connecting the Bluetooth multimeter (ZOYI ZT-300AB) to the sensor electrode to observe the resistance changes in real time on the phone through the software (e-Bull) developed by the merchant.

Washable and WVTR test of PMPP

Samples of 2 × 2 cm were placed into a beaker containing 70 mL of DI water and stirred by a magnetic stirrer (620 r·min⁻¹) for 15 min. Then, the samples were dried and the weight changes and resistance changes were measured. Water vapor transmission rate (WVTR) was tested with a protocol according to the American Society for Testing Materials (ASTM) E96-98. The samples were placed at the top of a bottle (containing 10 mL DI water) and the periphery was sealed with paraffin tape. At last, they were kept at

room temperature and weighed every 24 h. Data processing using formulas and criteria in Supplementary Note 1. SVTR was tested by using artificial perspiration and carried out at a temperature of 37 °C in an oven.

Biocompatibility evaluation of PMPP

In vitro cell culture of mouse cells (NIH-3T3) is performed by MTT assay according to ISO/EN 10993-5:1999 standards to explore the cell compatibility of the hybrid sponges. First, samples were irradiated under a UV lamp for 1 h. Then, samples were put into DMEM medium (material surface area/dipping medium = 3 cm²·mL⁻¹) and soaked in a 37 °C, 5% CO₂ incubator for 24 h to obtain extract liquid. Cultured adherent grown mouse cells (NIH-3T3) were supplemented with 100 μL/well. Five parallel experiments were performed for each set of material. After grouping treatment as described above, cells were incubated with extract liquid for 24 h following removing the medium. 10 μL of MTT solution (0.5 g·L⁻¹) were added to each well of the 96-well plate and incubated for a further 4 h and the supernatant was discarded. Then, 100 μL of DMSO were added to each well, lightly shaken for 10 min at room temperature and then incubated in an incubator for 15 min before removal. Finally, use a microplate reader (BioTekn) to the measure absorbance at 570 nm of each well. Data processing using formulas and criteria in Supplementary Note 2. Live/dead cells were stained with calcein and PI dye and cultivated 24 h. Then, discard the supernatant and wash cells three times with PBS. Finally, Confocal Laser Scanning Microscope (Leica SP8) was used to observe live/dead cells.

Sensing test of PMPPF

The sensing test was controlled by Dynamic mechanical analysis (DMA 3200) and resistance signals were collected by impedance tester (ModuLab XM MTS) in real time. Samples of 1.5 cm × 3 cm were used for stretch-sensing, while 1.5 cm × 1.5 cm for compress-sensing and 1.5 cm × 3 cm for bend-sensing. During the bending testing, the PMPPF was attached on a PDMS film and then the PDMS film was compressed to induce bending. In this case, the bending angle α was defined as the rotation angle from central axis of clamps. Finite element (FEM) simulations were performed with the Comsol 5.5. Parameter setting: Young's modulus of PMPP is 1 MPa and medical Film is 2 MPa. In pressure mode, two hard plates are introduced to PMPP's up and down; in stretch mode, the ends of the PMPPF are clamped; in bending mode, the PMPP is attached to the lateral side of a hard plate and curved outwards. Optical microscopy (VHX-200) was used to observe the process of samples stretching and compression.

Photothermal effect test of PMPPF

The sample was exposed to adjustable 808 nm infrared light (height 10 cm) and Xenon lamp (MC-XS500) (Height = 17 cm), the temperature of the lower surface was measured with a thermocouple (CEM DT-8891E). The light intensity was controlled by 808 nm multimode fiber laser (GX-808). The optical fiber irradiation area was amplified with a beam expansion lens ($d = 2$ cm). Surface temperature map were recorded using an infrared camera (Imager 8325). Environment temperature is controlled by temperature control mode of Rotary rheometer (Anton Paar, MCR 302).

Antibacterial activity test of PMPPF

Gram-negative bacteria (*E. coli*) and Gram-positive bacteria (*S. aureus*) were selected to evaluate the antibacterial properties of the samples. First, PMPPF was cut into 2 cm diameter circles and placed into a 24-well plate. Next, 50 μL of bacterial droplets suspended with PBS (~10⁶ CFU·mL⁻¹) were placed on each

sample. Then, Near-infrared light targets each well (height 10 cm) for an arranged irradiate time and power density. 0.45 mL PBS was added to each well for a total volume of 0.5 mL, followed by serially diluting each well six times at 1:10 (0.1 mL bacterial suspension in 0.9 mL PBS). Finally, 10 μ L of dilution was taken on the medium and grown in a 37 °C incubator for 24 h. The survival level was determined by the ratio of CFU·mL⁻¹ of the plate versus that of the corresponding blank control (set to 100%). It is worth mentioning that three parallel experiments were performed for each sample. Data processing using formulas and criteria in Supplementary Note 4.

Characterization

The surface morphologies of PU, PM, PMP, PMPP and bacterial were characterized by scanning electron microscopy (SEM, Sirion 200). Field emission transmission electron microscopy (FETEM) images of MXene nanosheets were recorded on a FETEM JEM-2100F with an accelerating voltage of 200 kV. The height morphology of MXene nanosheets was characterized by the atomic force microscope (AFM, dimension icon, Bruker). The crystalline phase characterization of the MXene and MAX was performed by X-ray diffraction (XRD) (SmartLab, Japan). Water contact angles were photographed with a digital single lens reflex camera and measured with Photoshop CS6. The Fourier transform infrared spectroscopy (FTIR) was tested using a Bruker alpha apparatus in ATR mode from 4000 to 650 cm⁻¹ using 24 scans at a resolution of 4 cm⁻¹. X-ray photoelectron spectra (XPS) were measured by Electron Spectroscopy (ESCALAB 250). Thermogravimetric analysis (TGA) was performed on a thermogravimeter (DTG-60H) heated from room temperature to 800 °C under N₂ condition at a heating rate of 10 °C·min⁻¹. The force-displacement curve for samples (0.57 mm thickness, 19 mm width and 30 mm length) was measured by Instron (E3000K8953) at a strain rate of 0.3 mm·s⁻¹.

DATA AVAILABILITY

All relevant data that support the findings of this study are available from authors upon reasonable request.

Received: 3 August 2022; Accepted: 7 November 2022;

Published online: 21 November 2022

REFERENCES

- Tomkins, C. Sports medicine and rehabilitation: a sport-specific approach. *JAMA J. Am. Med. Assoc.* **302**, 441 (2009).
- Dhillon, H., Dhillon, S. & Dhillon, M. S. Current concepts in sports injury rehabilitation. *Indian J. Orthop.* **51**, 529–536 (2017).
- Malliaropoulos, N., Mertyry, D., Tsitas, K., Papalada, A. & Maffuli, N. Active ankle range of motion assessment in elite track and field athletes: normative values. *Br. J. Sports Med.* **47**, e3 (2013).
- Lee, G. et al. User-interactive thermotherapeutic electronic skin based on stretchable thermochromic strain sensor. *Adv. Sci.* **7**, 2001184 (2020).
- Moon, D. I. et al. On-demand printing of wearable thermotherapy pad. *Adv. Healthc. Mater.* **9**, 1901575 (2020).
- Du, P. et al. A novel breathable flexible metallized fabric for wearable heating device with flame-retardant and antibacterial properties. *J. Mater. Sci. Technol.* **122**, 200–210 (2022).
- Liu, M. et al. Electronic textiles based wearable electrotherapy for pain relief. *Sens. Actuators, A* **303**, 111701 (2020).
- Deng, M. et al. Fall preventive gait trajectory planning of a lower limb rehabilitation exoskeleton based on capture point theory. *Front. Inform. Technol. Elect. Eng.* **20**, 1322–1330 (2019).
- Zadeh, A. et al. Predicting sports injuries with wearable technology and data analysis. *Inf. Syst. Front.* **23**, 1023–1037 (2021).
- Fonseca, S. T. et al. Sports injury forecasting and complexity: a synergetic approach. *Sports Med.* **50**, 1757–1770 (2020).
- Emery, C. A. & Pasanen, K. Current trends in sport injury prevention. *Best. Pract. Res., Clin. Rheumatol.* **33**, 3–15 (2019).
- Mendonça, L. D. M. et al. Sports injury prevention programmes from the sports physical therapist's perspective: An international expert Delphi approach. *Phys. Ther. Sport* **55**, 146–154 (2022).
- Luo, J., Gao, W. & Wang, Z. L. The triboelectric nanogenerator as an innovative technology toward intelligent sports. *Adv. Mater.* **33**, 2004178 (2021).
- Sahu, M. et al. Waste textiles as the versatile triboelectric energy-harvesting platform for self-powered applications in sports and athletics. *Nano Energy* **97**, 107208 (2022).
- Jeong, S. et al. Development of multi-angle fiber array for accurate measurement of flexion and rotation in human joints. *npj Flex. Electron.* **5**, 35 (2021).
- Yang, P. et al. Monitoring the degree of comfort of shoes in-motion using triboelectric pressure sensors with an ultrawide detection range. *ACS Nano* **16**, 4654–4665 (2022).
- Amjadi, M., Kyung, K. U., Park, I. & Sitti, M. Stretchable, skin-mountable, and wearable strain sensors and their potential applications: a review. *Adv. Funct. Mater.* **26**, 1678–1698 (2016).
- Chen, G. et al. Electronic textiles for wearable point-of-care systems. *Chem. Rev.* **122**, 3259–3291 (2022).
- Wang, C., Shirzaei Sani, E. & Gao, W. Wearable bioelectronics for chronic wound management. *Adv. Funct. Mater.* **32**, 2111022 (2022).
- Li, X. et al. A self-supporting, conductor-exposing, stretchable, ultrathin, and recyclable kirigami-structured liquid metal paper for multifunctional e-skin. *ACS Nano* **16**, 5909–5919 (2022).
- Su, T. et al. MXene/cellulose nanofiber-foam based high performance degradable piezoresistive sensor with greatly expanded interlayer distances. *Nano Energy* **87**, 106151 (2021).
- Liang, X. et al. Hydrophilic, breathable, and washable graphene decorated textile assisted by silk sericin for integrated multimodal smart wearables. *Adv. Funct. Mater.* **32**, 2200162 (2022).
- Wang, H. et al. A soft and stretchable electronics using laser-induced graphene on polyimide/PDMS composite substrate. *npj Flex. Electron.* **6**, 26 (2022).
- Tao, K. et al. Ultra-sensitive, deformable, and transparent triboelectric tactile sensor based on micro-pyramid patterned ionic hydrogel for interactive human-machine interfaces. *Adv. Sci.* **9**, 2104168 (2022).
- Qu, X. et al. Fingerprint-shaped triboelectric tactile sensor. *Nano Energy* **98**, 107324 (2022).
- Zhang, C., Zhang, C., Wu, X., Ping, J. & Ying, Y. An integrated and robust plant pulse monitoring system based on biomimetic wearable sensor. *npj Flex. Electron.* **6**, 43 (2022).
- Xu, H. et al. Flexible tensile strain-pressure sensor with an off-axis deformation-insensitivity. *Nano Energy* **99**, 107384 (2022).
- Zhang, Y. et al. Multi-layer printable lithium ion micro-batteries with remarkable areal energy density and flexibility for wearable smart electronics. *Small* **18**, 2104506 (2022).
- Li, L. et al. Moisture-driven power generation for multifunctional flexible sensing systems. *Nano Lett.* **19**, 5544–5552 (2019).
- Wang, M. et al. Leaf-meridian bio-inspired nanofibrous electronics with uniform distributed microgrid and 3D multi-level structure for wearable applications. *npj Flex. Electron.* **6**, 34 (2022).
- Jeong, S. Y. et al. Foldable and washable textile-based OLEDs with a multifunctional near-room-temperature encapsulation layer for smart e-textiles. *npj Flex. Electron.* **5**, 15 (2022).
- Gong, M. et al. Knittable and sewable spandex yarn with nacre-mimetic composite coating for wearable health monitoring and thermo- and antibacterial therapies. *ACS Appl. Mater. Int.* **13**, 9053–9063 (2021).
- Li, Y. Q. et al. Multifunctional wearable device based on flexible and conductive carbon sponge/polydimethylsiloxane composite. *ACS Appl. Mater. Int.* **8**, 33189–33196 (2016).
- Zhou, Z., Song, Q., Huang, B., Feng, S. & Lu, C. Facile fabrication of densely packed Ti₃C₂X MXene/nanocellulose composite films for enhancing electromagnetic interference shielding and electro-/photothermal performance. *ACS Nano* **15**, 12405–12417 (2021).
- Cao, Y. M. et al. Smart textiles based on MoS₂ hollow nanospheres for personal thermal management. *ACS Appl. Mater. Interfaces* **13**, 48988–48996 (2021).
- Choi, S. et al. Stretchable heater using ligand-exchanged silver nanowire nanocomposite for wearable articular thermotherapy. *ACS Nano* **9**, 6626–6633 (2015).
- Yang, D. et al. Self-healing and elastic triboelectric nanogenerators for muscle motion monitoring and photothermal treatment. *ACS Nano* **15**, 14653–14661 (2021).
- Zhao, Y. et al. Skin-inspired antibacterial conductive hydrogels for epidermal sensors and diabetic foot wound dressings. *Adv. Funct. Mater.* **29**, 1901474 (2019).
- Ho, D. H., Choi, Y. Y., Jo, S. B., Myoung, J. & Cho, J. H. Sensing with MXenes: progress and prospects. *Adv. Mater.* **33**, 2005846 (2021).
- Sang, M. et al. Flexible and lightweight melamine sponge/MXene/polyborosiloxane (MSMP) hybrid structure for high-performance electromagnetic

- interference shielding and anti-impact safe-guarding. *Compos., Part B* **211**, 108669 (2021).
41. Li, W. et al. Dual-mode biomimetic soft actuator with electrothermal and magneto-responsive performance. *Compos., Part B* **238**, 109880 (2022).
 42. Zeng, Z. et al. Porous and ultra-flexible crosslinked MXene/polyimide composites for multifunctional electromagnetic interference shielding. *Nano-Micro Lett.* **14**, 59 (2022).
 43. Li, Q. et al. Flexible conductive MXene/cellulose nanocrystal coated nonwoven fabrics for tunable wearable strain/pressure sensors. *J. Mater. Chem. A* **8**, 21131–21141 (2020).
 44. Yang, D. et al. Flexible transparent polypyrrole-decorated MXene-based film with excellent photothermal energy conversion performance. *ACS Appl. Mater. Int.* **13**, 8909–8918 (2021).
 45. Xu, W. et al. Nacre-inspired tunable strain sensor with synergistic interfacial interaction for sign language interpretation. *Nano Energy* **90**, 106606 (2021).
 46. Sang, M. et al. Flexible polyvinylidene fluoride (PVDF)/MXene (Ti₃C₂T_x)/polyimide (PI) wearable electronic for body monitoring, chemotherapy and electromagnetic interference shielding. *Compos., Part A* **153**, 106727 (2022).
 47. Yang, M. et al. High-performance flexible pressure sensor with a self-healing function for tactile feedback. *Adv. Sci.* **9**, 2200507 (2022).
 48. Qin, S. et al. Development and applications of MXene-based functional fibers. *ACS Appl. Mater. Int.* **13**, 36655–36669 (2021).
 49. Shi, M. et al. Ti₃C₂T_x MXene-decorated nanoporous polyethylene textile for passive and active personal precision heating. *ACS Nano* **15**, 11396–11405 (2021).
 50. Lo, L. et al. A soft sponge sensor for multimodal sensing and distinguishing of pressure, strain, and temperature. *ACS Appl. Mater. Int.* **14**, 9570–9578 (2022).
 51. Li, Y. et al. Ultrasensitive pressure sensor sponge using liquid metal modulated nitrogen-doped graphene nanosheets. *Nano Lett.* **22**, 2817–2825 (2022).
 52. Zhang, D. et al. Multifunctional superelastic graphene-based thermoelectric sponges for wearable and thermal management devices. *Nano Lett.* **22**, 3417–3424 (2022).
 53. Zhang, Y. et al. MXene printing and patterned coating for device applications. *Adv. Mater.* **32**, 1908486 (2020).
 54. Zhang, S. et al. Polydopamine functional reduced graphene oxide for enhanced mechanical and electrical properties of waterborne polyurethane nanocomposites. *J. Coat. Technol. Res.* **15**, 1333–1341 (2018).
 55. Qing, W. et al. Bioinspired dielectric film with superior mechanical properties and ultrahigh electric breakdown strength made from aramid nanofibers and alumina nanoplates. *Polymers* **13**, 3093 (2021).
 56. Wang, H. et al. High-performance foam-shaped strain sensor based on carbon nanotubes and Ti₃C₂T_x MXene for the monitoring of human activities. *ACS Nano* **15**, 9690–9700 (2021).
 57. Liu, Z. et al. Highly breathable and stretchable strain sensors with insensitive response to pressure and bending. *Adv. Funct. Mater.* **31**, 2007622 (2021).
 58. Wang, Y. et al. Three-layer core-shell Ag/AgCl/PEDOT: PSS composite fibers via a one-step single-nozzle technique enabled skin-inspired tactile sensors. *Chem. Eng. J.* **442**, 136270 (2022).
 59. Pang, Q. et al. Smart flexible electronics-integrated wound dressing for real-time monitoring and on-demand treatment of infected wounds. *Adv. Sci.* **7**, 1902673 (2020).
 60. Zhao, X. et al. Self-assembled core-shell polydopamine@MXene with synergistic solar absorption capability for highly efficient solar-to-vapor generation. *Nano Res.* **13**, 255–264 (2022).
 61. Zhao, W. et al. AgNWs/MXene derived multifunctional knitted fabric capable of high electrothermal conversion efficiency, large strain and temperature sensing, and EMI shielding. *J. Alloy. Compd.* **923**, 166471 (2022).
 62. Zhao, L. et al. Tissue-like sodium alginate-coated 2D MXene-based flexible temperature sensors for full-range temperature monitoring. *Adv. Mater. Technol.* **7**, 2101740 (2022).
 63. Xu, Y. et al. Rough surface NiFe₂O₄@Au/polydopamine with a magnetic field enhanced photothermal antibacterial effect. *Chem. Eng. J.* **437**, 135282 (2022).
 64. Chantapakul, T. et al. Manothermosonication: inactivation of *Escherichia coli* and *Staphylococcus aureus*. *J. Food Eng.* **246**, 16–24 (2019).
 65. Rosenkranz, A. et al. Laser-mediated antibacterial effects of few- and multi-layer Ti₃C₂T_x MXenes. *Appl. Surf. Sci.* **567**, 150795 (2021).

ACKNOWLEDGEMENTS

Financial supports from the National Natural Science Foundation of China (Grant Nos. 12072338, 11972343, 12132016, 12202435), the Anhui's Key R&D Program of China (202104a05020009), the Fundamental Research Funds for the Central Universities (WK2480000007) and the Aviation Science Foundation of China (20200029079004), are gratefully acknowledged.

AUTHOR CONTRIBUTIONS

Conceptualization: X.W. Methodology: X.W. Investigation: X.W., Y.T., S.P., X.F., C.L., Y.X., J.W., L.L., T.L. Visualization: X.W., Y.T., S.P., X.F., C.L., Y.X., J.W., M.S., L.L., T.L. Supervision: S.X., X.G. Writing-original draft: X.W. Writing-review & editing: X.W., S.X., X.G.

COMPETING INTERESTS

The authors declare no competing interests.

ADDITIONAL INFORMATION

Supplementary information The online version contains supplementary material available at <https://doi.org/10.1038/s41528-022-00228-x>.

Correspondence and requests for materials should be addressed to Xinglong Gong or Shouhu Xuan.

Reprints and permission information is available at <http://www.nature.com/reprints>

Publisher's note Springer Nature remains neutral with regard to jurisdictional claims in published maps and institutional affiliations.



Open Access This article is licensed under a Creative Commons Attribution 4.0 International License, which permits use, sharing, adaptation, distribution and reproduction in any medium or format, as long as you give appropriate credit to the original author(s) and the source, provide a link to the Creative Commons license, and indicate if changes were made. The images or other third party material in this article are included in the article's Creative Commons license, unless indicated otherwise in a credit line to the material. If material is not included in the article's Creative Commons license and your intended use is not permitted by statutory regulation or exceeds the permitted use, you will need to obtain permission directly from the copyright holder. To view a copy of this license, visit <http://creativecommons.org/licenses/by/4.0/>.

© The Author(s) 2022